

Macroscopic Heterogeneities in Electroosmotic and Pressure-Driven Flow through Fixed Beds at Low Column-to-Particle Diameter Ratio

Ulrich Tallarek,* Tom W. J. Scheenen, and Henk Van As

Laboratory of Molecular Physics and Wageningen NMR Centre, Department of Biomolecular Sciences, Wageningen University, Dreijenlaan 3, 6703 HA Wageningen, The Netherlands

Received: April 3, 2001; In Final Form: June 25, 2001

By using dynamic NMR microscopy with 40 μm spatial resolution we have demonstrated the existence of specific wall effects in electroosmotic and pressure-driven flows through a fixed bed at low column-to-particle diameter ratio. While the geometrical wall effect encountered in pressure-driven flow through the packed capillary is due to the radial distribution of interstitial porosity, with increasing void space closer to the wall, the electrokinetic wall effect is caused by different values of the zeta-potential associated with the inner surface of the capillary and those of the particles. It is shown that these wall effects are very systematic along the column axis for both types of fluid flow. They can cause a persistent (i.e., long-time) disequilibrium in the axial dispersion behavior, and associated correlation lengths of the flow field may cover the total radius of the packed capillary needing trans-column equilibration. The characteristic times of these macroscopic flow heterogeneities in electroosmotic and pressure-driven flows exceed by far those of the stagnant mobile phase mass transfer in the bed as we show by complementary pulsed field gradient NMR measurements.

Introduction

Due to the nonuniform radial distribution of voidage, permeability, and interstitial velocity in a critical region close to the wall,^{1–13} the column diameter (d_c) to particle diameter (d_p) ratio may influence transport properties in fixed-bed catalytic reactors and chromatographic columns. It has already been shown in early studies and for uniform spheres with a smooth surface that the interstitial porosity (ϵ_{inter}) starts with a maximum value of unity at the column wall and then displays damped oscillations with a period close to d_p over a distance of 4–5 d_p into the bulk of the bed until the void fraction reaches values typical for random close packings of particles ($\epsilon_{\text{inter}} = 0.38 - 0.4$, Figure 1).^{14–16} This behavior is explained by a decrease of packing order as the distance from the wall increases. To calculate the isothermal steady-flow profiles from a radial porosity distribution function $\epsilon_{\text{inter}}(r)$, which sensitively depends on particle shape, size distribution, and surface roughness, Vortmeyer and co-workers¹³ employed a classical model based on the Brinkman equation.¹⁷ They extended it to higher flow rates by adding an inertia term (incorporating the Ergun pressure-loss relation¹⁸)

$$\frac{\partial p}{\partial z} = -150 \eta_f \frac{(1 - \epsilon_{\text{inter}}(r))^2}{\epsilon_{\text{inter}}(r)^3} \frac{v}{d_p^2} - 1.75 \rho_f \frac{(1 - \epsilon_{\text{inter}}(r))}{\epsilon_{\text{inter}}(r)^3} \frac{v^2}{d_p} + \frac{\eta_{\text{eff}}}{r} \frac{\partial}{\partial r} \left(r \frac{\partial v}{\partial r} \right) \quad (1)$$

An effective viscosity η_{eff} is used to compensate the failure of the pressure-loss relation close to the wall,¹³ while η_f and ρ_f are the fluid dynamic viscosity and density. The consequences

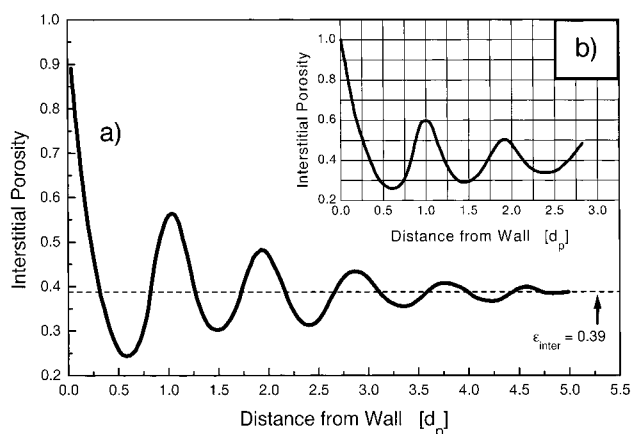


Figure 1. The radial porosity distribution function $\epsilon_{\text{inter}}(r)$ for fixed beds of monodisperse particles with perfect spherical shape and smooth surface. Experimental data for different column-to-particle diameter ratios: (a) $d_c/d_p = 14.1$, (b) $d_c/d_p = 5.6$ (after Benenati and Brosilow¹⁵).

of this geometrical wall effect for the flow heterogeneity, axial dispersion, and particle-to-fluid heat and mass transfer may be particularly severe at aspect ratios $\psi = d_c/d_p$ below 15 where the wall region occupies a substantial fraction of the total column.^{19–22} For larger aspect ratios it was found that (within limits of experimental precision) the dispersion in beds of spheres is independent of ψ .²³

A second wall effect has been shown to exist in analytical and preparative-scale columns ($\psi \gg 100$), which is probably caused by friction between the bed and the column wall.^{24–26} This effect strongly depends on the packing procedure and operational characteristics. It is related to the relatively high compressibility of pulverulent materials and complex distribution of axial and radial stress during the compression of the bed.^{27,28} For small slurry-packed columns it was found that the packing density is higher near the column exit and wall than in the upper and central regions.²⁹ The fractional volume affected by this

* To whom correspondence should be addressed. Present address: Lehrstuhl für Chemische Verfahrenstechnik, Otto-von-Guericke Universität Magdeburg, Universitätsplatz 2, 39106 Magdeburg, Germany. Phone: +49 (0)391 67-18644. Fax: +49 (0)391 67-12028. E-mail: ulrich.tallarek@vst.uni-magdeburg.de.

interaction (compared to the first, purely geometrical effect) is much larger and may extend to about $50 d_p$ into the bulk of the bed.^{30,31} It may be even thicker for preparative columns.³² Both wall effects and the interplay as a function of ψ are critical in chromatography since radial variations of transport properties have a far more serious effect on column performance than do axial ones.

In sharp contrast to the radial porosity distribution function and its influence on the velocity heterogeneity in pressure-driven flows (wall effects in particular), it is the radial distribution of the zeta-potential (ζ) at the solid–liquid interface, i.e., a variation of the electrokinetic potential at the hypothetical plane of shear,^{33,34} that determines the flow profile of an electrokinetically driven mobile phase through fixed beds. Electroosmotic flow (EOF) originates in the electrical double layer which exists when the liquid is in contact with charged surfaces such as those of ion exchange media.

Capillary electrochromatography (CEC) is typically carried out in capillary columns (i.d. $< 150 \mu\text{m}$) packed with $3\text{--}5 \mu\text{m}$ porous adsorbent particles (thus, $\psi < 50$). Electric fields of up to 100 kV/m are applied to move a buffer solution and solute through the medium by electroosmosis (and electrophoresis if the solute is charged).^{35–39} Basically CEC is a hybrid between capillary electrophoresis (CE) and capillary high performance liquid chromatography (CHPLC), as the partitioning between two phases (e.g., a differential adsorption on the particles surfaces) still constitutes one major factor, as in CHPLC.^{40,41} Concerning the interstitial flow characteristics, mainly two aspects may contribute to an improved efficiency of the EOF in chromatographic separations (as compared to pressure-driven flows).⁴² They largely reflect implications of the parallel-pore model for a porous medium, although the exact microscopic details of the EOF are more complex than it suggests.^{43,44} It is expected that the velocity distribution in a single pore of the network carries features of a plug-like profile which is predicted^{45–49} and has also been observed^{50,51} for pure electrokinetic flow in open capillaries, if the electrical double layer thickness (κ^{-1}) is small compared to the pore radius (r_{pore}). Second, with thin double layers ($\kappa r_{\text{pore}} \gg 1$), the average velocity in a pore is relatively independent of the pore radius and the actual porosity distribution has largely lost its impact on a flow heterogeneity.⁴⁶ This aspect is supported by observing that the average EOF in packed capillaries is hardly influenced by the particle diameter.⁵²

For the EOF through fixed beds at a low aspect ratio ($\psi < 50$), however, it has been shown theoretically by Rathore and Horváth⁵³ and Liapis and Grimes⁵⁴ that the excess zeta-potential $\zeta_{\text{ex}} = (\zeta_w - \zeta_p)$, i.e., the difference between ζ associated with the capillary surface (ζ_w) and the particles surface (ζ_p), can have a deleterious effect on the column cross-sectional flow profile and average velocity. In general, the electrokinetic (and chromatographic) properties of these surfaces are quite different. Using the mathematical model constructed and solved by Liapis and Grimes,⁵⁴ the influence of the capillary wall (via ζ_w) on the radial distribution of the EOF can be expressed by (cf. Figure 2)

$$\frac{v_{\text{eo}}(r)}{v_p} = 1 + \left(\frac{\zeta_w}{\zeta_p} - 1 \right) \frac{I_0(\beta r/d_p)}{I_0(\beta r_{\text{eff}}/d_p)} \quad (2)$$

with $0 \leq r \leq r_c - 7/\kappa \equiv r_{\text{eff}}$ and where I_0 is the zero-order modified Bessel function of the first kind and r_{eff} is an effective capillary radius that accounts for the no-slip condition at the inner wall of the column, i.e., $v_{\text{eo}}(r_c) = 0$.⁵⁴ The constant β

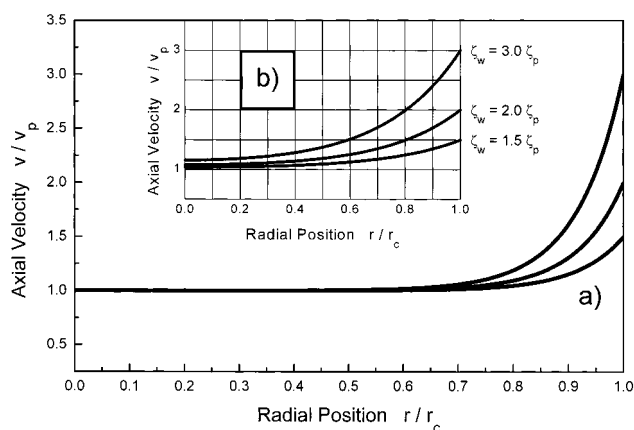


Figure 2. Radial distribution of the EOF velocity in packed beds (normalized by v_p , the velocity that is generated locally at the particle's external surface) for different values of ζ_w/ζ_p and aspect ratios, based on eq 2. (a) $d_c/d_p = 15$; (b) $d_c/d_p = 5$.

characterizes the overall permeability of the bed and can be evaluated from the following relationship⁵⁵

$$\beta = \left(\frac{9}{2} (1 - \epsilon_{\text{inter}}) \Phi \right)^{1/2} \quad (3)$$

The dimensionless parameter Φ depends on the drag force that is provided by a spherical porous (permeable) particle in the packing.^{54,55} As demonstrated in Figure 2, both the excess zeta-potential and the aspect ratio contribute to the actual EOF profile. These effects are too significant to neglect in current CEC practice with $\psi < 50$ unless $\zeta_w \approx \zeta_p$. Although one of the ultimate goals,^{52,56} the use of submicron particles in CEC columns ($\psi > 100$) is still far from a routine application.

The present work was motivated by a very discrete influence of the column wall on the fluid dynamics of electroosmotic and pressure-driven flow fields in fixed beds. Because these wall effects are aggravated at a low aspect ratio, they are relevant to (electro)separation science when $\psi < 50$. We used pulsed field gradient (PFG) NMR and dynamic NMR microimaging to assign the origin and severe consequences of a systematic velocity heterogeneity to specific wall effects that are expected in either type of fluid flow. Our first direct documentation of wall effects for the EOF through a bed of charged porous particles in a charged capillary actually addresses the importance of that issue for a further optimization in CEC column engineering and surface chemistry.

Theoretical Background

Dispersion in Fixed Beds. In the asymptotic (long-time) limit, dispersion of a passive tracer in single-phase incompressible fluid flow through random porous media can be described by the local, averaged convection-diffusion equation in form of a macroscopic Fick law with an effective, i.e., constant dispersion tensor (\mathbf{D})⁵⁷

$$\frac{\partial \langle c \rangle}{\partial t} + \mathbf{V} \cdot \nabla \langle c \rangle = \mathbf{D} \cdot \nabla^2 \langle c \rangle \quad (4)$$

It assumes implicitly that the dispersion process is Gaussian where $\langle c \rangle$ denotes the average concentration of tracer molecules and \mathbf{V} , the mean interstitial velocity, is an average over the local (instantaneous) velocities, \mathbf{v} . Then, \mathbf{D} can be expressed by the autocorrelation function of the fluctuations in the velocity field⁵⁸

$$\mathbf{D} = \lim_{t \rightarrow \infty} \int_0^t \langle [\mathbf{v}(0) - \mathbf{V}] \cdot [\mathbf{v}(t') - \mathbf{V}] \rangle dt' \quad (5)$$

Actually, eq 5 reflects the Lagrangian description of fluid motion since \mathbf{D} is determined by an integral over the whole path of a molecule (in the limit of long times) and not by an average of local values as in the Eulerian approach, which involves an instantaneous picture of all the points in the flow field.⁵⁹ Eulerian (\mathbf{D}_E) and Lagrangian (\mathbf{D}_L) definitions give the same effective dispersion tensor \mathbf{D} with the exception of possible antisymmetric components of \mathbf{D}_E arising in media whose structures lack a reflectional symmetry (since $\mathbf{D}_L = \text{sym } \mathbf{D}_E$).⁶⁰ When the porous medium is isotropic on a macroscopic scale, \mathbf{D} can be decomposed into axial and transverse components, i.e., those parallel (D_a) and perpendicular (D_t) to \mathbf{V} , and the convection-diffusion equation becomes

$$\frac{\partial \langle c \rangle}{\partial t} + \mathbf{V} \cdot \nabla \langle c \rangle = D_a \frac{\partial^2 \langle c \rangle}{\partial z^2} + D_t \nabla_t^2 \langle c \rangle \quad (6)$$

In the preasymptotic dispersion regime (at intermediate times) and for heterogeneous porous media, in general, when the average displacements of tracer molecules are comparable to the spatial fluctuations in the velocity field and \mathbf{D} is time-dependent, the nonlocal dispersion formalism due to Koch and Brady could be adapted.^{61,62} Although this transport theory was originally developed for dilute systems of noninteracting spheres, experimental evidence for the applicability of that approach to random close packings has been recently presented by Ding and Candela.⁶³ \mathbf{D} can be considered as a nonlocal generalization of the traditional (or Fickian) diffusivity, depending on the tracer particle shifts in space and time^{61,62}

$$\mathbf{D} = \langle [\mathbf{v}(\mathbf{r}', t') - \mathbf{V}] P(\mathbf{r}', t'/\mathbf{r}, t) [\mathbf{v}(\mathbf{r}, t) - \mathbf{V}] \rangle \quad (7)$$

In this respect, $P(\mathbf{r}', t'/\mathbf{r}, t)$ is the transition probability (or propagator) of finding a molecule at \mathbf{r}' at time t' given that it was at \mathbf{r} at time t . The nonlocal dispersion theory of Koch and Brady may be used to obtain the average concentration response to any source, regardless of its length scale or time scale, and allows to recognize non-Fickian behavior simply as dispersion processes that have not reached their asymptotic, i.e., (pseudo)-diffusive limits.

Analysis of Motion via Magnetic Field Gradients. The general analysis of fluid transport in fixed beds based on magnetic field gradients has found considerable potential (see Seymour and Callaghan⁶⁴ for a detailed description) and it includes the axial and transverse dispersion characteristics,^{64–68} structure-flow and dispersion correlations,^{69,70} scaling behavior,^{71,72} and the stagnant mobile phase mass transfer kinetics.^{73,74} In the context of dispersion, PFG-NMR can be used to obtain directly the nuclear spin (hence, a molecular) displacement probability distribution of the fluid (tracer) molecules in both electroosmotic and pressure-driven flows through packed capillaries, on an experimental time scale between 15 ms and ca. 1.5 s. The motion-encoding field gradients of amplitude (and direction) \mathbf{g} and duration δ define a vector in \mathbf{q} -space, i.e., $2\pi\mathbf{q} = \gamma\delta\mathbf{g}$ ^{75–77} and γ is the gyromagnetic ratio of the nucleus. Introducing an averaged propagator, $P_{av}(\mathbf{R}, \Delta)$,^{78,79} as the probability that any molecule (e.g., $^1\text{H}_2\text{O}$) travels a net distance $\mathbf{R} = \mathbf{r}'(t') - \mathbf{r}(t)$ over the experimental observation time $\Delta = (t' - t)$, we get a direct Fourier relation between $P_{av}(\mathbf{R}, \Delta)$ and the normalized signal, $E(\mathbf{q}, \Delta)$, acquired in the \mathbf{q} -space, characterizing a PFG-NMR measurement in the narrow gradient pulse limit ($\delta \ll \Delta$)^{80,81}

$$E(\mathbf{q}, \Delta) = \frac{S(\mathbf{q}, \Delta)}{S(0, \Delta)} = \int P_{av}(\mathbf{R}, \Delta) \exp(i2\pi\mathbf{q} \cdot \mathbf{R}) d\mathbf{R} \quad (8)$$

Thus, \mathbf{q} -space is reciprocal to the (dynamic) displacement space \mathbf{R} and $P_{av}(\mathbf{R}, \Delta)$ is recovered by Fourier transformation of $E(\mathbf{q}, \Delta)$ with respect to \mathbf{q} . The averaged propagator, $P_{av}(\mathbf{R}, \Delta)$, of the fluid molecules is related to their conditional probability, $P(\mathbf{r}', t'/\mathbf{r}, t)$, by the probability (i.e., nuclear spin) density, $\rho(\mathbf{r})$, for the original positions

$$P_{av}(\mathbf{R}, \Delta) = \int \rho(\mathbf{r}) P(\mathbf{r}', t'/\mathbf{r}, t) d\mathbf{r} \quad (9)$$

In columns packed with porous particles we may distinguish (via the net displacements over time Δ) between convective-diffusive interparticle and purely diffusive fluid molecules that have remained in the deep stagnant pools inside the particles.⁷⁴ When on the experimental time scale both intraparticle diffusion and interparticle dispersion are Gaussian processes, the amplitude modulation of $S(\mathbf{q}, \Delta)$ is given by

$$S(\mathbf{q}, \Delta) = \sum_{n=1}^2 A_n(\Delta) \exp\left[-4\pi^2 \mathbf{q}^2 D_n \left(\Delta - \frac{\delta}{3}\right)\right] \quad (10)$$

$A_n(\Delta)$ represents the number of moving and stagnant fluid molecules. By recording $A_{intra}(\Delta)$ it is possible to monitor the fictitious emptying of the porous particles and characterize stagnant mobile phase mass transfer and its contribution to hold-up dispersion in the packed bed. The use of eq 10 assumes that adequate correction has been made for the nuclear spin–lattice (T_1) and spin–spin (T_2) relaxation times.⁷⁴

In the context of our present PFG-NMR measurements, typical average axial displacements of the fluid molecules in both electroosmotic and pressure-driven flows through the packed capillary are not much larger than the spatial scale of the actual flow heterogeneity. Thus, the long-time limit of the apparent (transient) axial dispersion coefficient $D_{ap,a}$ taken with respect to the correlation time of the velocity fluctuations is not reached on the intrinsic experimental time scale. In this case, the low- \mathbf{q} limit of $E(\mathbf{q}, \Delta)$, corresponding to long-range displacements of fluid molecules in view of eq 8, may be analyzed to estimate $D_{ap,a}$. It has been shown by Callaghan and Stepišnik⁸² that the initial slope of the amplitude modulation of $E(\mathbf{q}, \Delta)$ can be expressed as

$$\lim_{\mathbf{q} \rightarrow 0} \frac{\partial}{\partial \mathbf{q}^2} \log|E(\mathbf{q}, \Delta)| = -4\pi^2 D_a(\Delta) \Delta \quad (11)$$

Although eq 11 is exact only in the case that the distribution of corresponding displacements is Gaussian, this asymptotic analysis with $4\pi^2 \mathbf{q}^2 D_a(\Delta) \Delta \ll 1$ provides a good working definition for the apparent (time-dependent) dispersion coefficient, i.e., $D_a(\Delta) \approx D_{ap,a}$.⁶⁴ In the long-time limit, this quantity corresponds to the effective (time-independent) dispersion coefficient that is defined by eq 6, i.e., $D_a(\Delta) \equiv D_a$. Then, when the exchange between mobile phase velocity extremes including intraparticle mass transfer is complete, $P_{av}(\mathbf{R}, \Delta)$ becomes a Gaussian and eq 10 has reduced to a single exponent containing D_a .

When in addition to the motion-encoding field gradients \mathbf{g} also spatial localization gradients of amplitude (and direction) \mathbf{G} and duration λ are applied, the acquired signal is modulated in \mathbf{q} -space and \mathbf{k} -space ($2\pi\mathbf{k} = \gamma\lambda\mathbf{G}$)^{82–84}

$$S(\mathbf{q}, \mathbf{k}) = \int \rho(\mathbf{r}) \int P_{\text{av}}(\mathbf{R}, \Delta) \exp(i2\pi \mathbf{q} \cdot \mathbf{R}) d\mathbf{R} \exp(i2\pi \mathbf{k} \cdot \mathbf{r}) d\mathbf{r} = \int \rho(\mathbf{r}) E(\mathbf{q}, \mathbf{r}, \Delta) \exp(i2\pi \mathbf{k} \cdot \mathbf{r}) d\mathbf{r} \quad (12)$$

Thus, \mathbf{k} -space is reciprocal to the (static) image space \mathbf{r} and $P_{\text{av}}(\mathbf{R}, \Delta)$ is implicitly a function of the pixel coordinate \mathbf{r} . Double inverse Fourier transformation of $S(\mathbf{k}, \mathbf{q})$ with respect to both \mathbf{k} and \mathbf{q} returns $\rho(\mathbf{r})P_{\text{av}}(\mathbf{R}, \Delta)$. Normalizing this function by the image density $\rho(\mathbf{r})$ acquired with $\mathbf{q} = 0$, $P_{\text{av}}(\mathbf{R}, \Delta)$ can be reconstructed for each pixel of the image. This dynamic NMR imaging (eq 12) naturally contains elements of both a Lagrangian (via motion-encoding) and Eulerian (via the spatial localization) information encoding.⁶⁴

Experimental Section

Capillary (Electro)Chromatography. The 250 μm i.d. (365 μm o.d.) cylindrical fused-silica capillary (Polymicro Technologies, Phoenix, AZ) was slurry-packed⁸⁵ with spherical-shaped, strong cation-exchange particles ($d_p = 50 \mu\text{m}$, thus $\psi = 5$) at pressures up to 100 bar. These particles (POROS HS from PerSeptive Biosystems, Framingham, MA) have a high density of sulphopropyl groups (i.e., permanent charges over a wide range of pH) at their surface which provide the basis for an electrical double layer at the solid–liquid interface and the generation of an EOF through the fixed bed, in addition to the EOF being generated at the inner surface of the capillary due to the silanol groups of the fused-silica wall.³⁴ The final bed length was 20 cm. A degassed 10^{-3} M sodium tetraborate buffer solution (pH 9.13) was used as the mobile phase in all our experiments, usually run in the creeping laminar flow regime with Reynolds numbers of the order of 0.05.⁵⁹ For the measurements requiring a steady EOF in the packed capillary, the electrodes of a modular CE instrument operating from 0 to 30 kV and up to 0.2 mA (Fa. Grom, Herrenberg-Kayh, Germany) were connected to the column by a home-built PEEK block with flow splitter and a buffer vessel through open fused-silica capillary segments.⁵¹ An integrated HPLC pump could be used for pressure-driven flows. Electrical field strengths and currents typically involved were around 35 kV/m and 20 μA , respectively.

Nuclear Magnetic Resonance. The ^1H NMR measurements were made at 30.7 MHz on an electromagnet (Bruker, Karlsruhe, Germany) interfaced with a SMIS console (Surrey Medical Imaging Systems, Guildford, U.K.) and an actively shielded gradient system (Doty Scientific, Columbia, SC) providing magnetic field gradients of up to 0.6 T/m. The packed capillary was fixed within a home-built radio frequency (r.f.) insert⁵¹ based on a 1.5 mm i.d. and 11 mm long solenoidal r.f. coil which allows a convenient sample access in the magnet. For spatially nonresolved measurements of $P_{\text{av}}(\mathbf{R}, \Delta)$ we used the stimulated echo sequence of the PFG-NMR methodology,⁸⁴ with Δ up to 1.5 s. $S(\mathbf{q}, \Delta)$ is generally acquired with a constant gradient pulse duration ($\delta = 2.5$ ms, $\delta \ll \Delta$), but incremented gradient amplitude \mathbf{g} by taking 40 \mathbf{q} -steps in the range of $\pm \mathbf{q}_{\text{max}}$ and up to 64 signal averages at each value of \mathbf{q} . Echo signals were acquired on-resonance and phased individually to extract the net amplitude modulation of $S(\mathbf{q}, \Delta)$. The dispersion coefficient is characterized in the low- \mathbf{q} limit, with $4\pi^2 \mathbf{q}^2 D_a(\Delta) \Delta \ll 1$ (cf. eqs 10 and 11). All calculations were made by using IDL (Interactive Data Language, Research Systems Inc., Boulder, CO).

For the microimaging of molecular displacements in the packed capillary, we implemented a pulse sequence that combines motion-encoding pulsed field gradients with a multiple

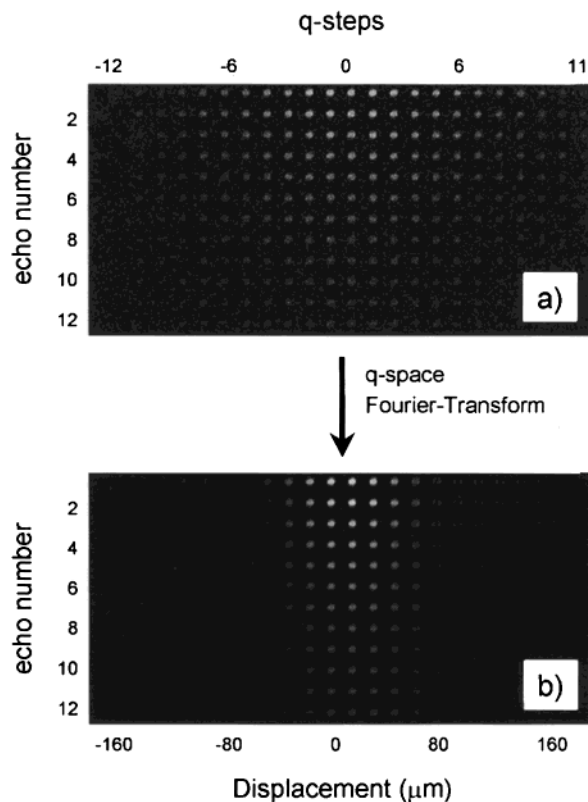


Figure 3. Multiecho PFG-NMR imaging experiment after Fourier transformation of the data with respect to \mathbf{k} . (a) 24×12 images of the packed capillary (24 \mathbf{q} -steps and 12 echoes) demonstrating the modulation of the complex signals real part depending on \mathbf{q} (horizontally) and echo number (vertically). (b) 24 images after zero filling in \mathbf{q} -space from 24 to 72 steps and Fourier transformation with respect to \mathbf{q} . The horizontal axis represents displacement space. Experimental parameters: $20 \times 20 \times 12 \times 24$ matrix; 0.8 mm field of view; 6.0 mm slice thickness; 0.8 s repetition time; \mathbf{g}_{max} , 0.31 T/m, $\delta = 2.3$ ms; $\Delta = 17.5$ ms; and echo time in train, 5.2 ms.

spin–echo imaging module.⁸⁶ It is the unique feature of this approach that not only an amplitude attenuation but also phase-information is maintained over the whole echo-train at each value of \mathbf{q} . Figure 3 illustrates the information of the multiecho PFG-NMR experiment after Fourier transformation of $S(\mathbf{k}, \mathbf{q})$ with respect to \mathbf{k} . Horizontally shown in Figure 3a is the modulation of the real part of $\rho(\mathbf{r})S(\mathbf{q})$ as a function of \mathbf{q} , whereas the signal decay in the echo-train is displayed vertically. After Fourier transformation of $\rho(\mathbf{r})S(\mathbf{q})$ with respect to \mathbf{q} (zero-filling of the data is possible here), we obtain $\rho(\mathbf{r})P_{\text{av}}(\mathbf{R}, \Delta)$ in Figure 3b. The signal decay in the echo-train is usually characterized by T_2 , but with a used nominal in-plane resolution of $40 \times 40 \mu\text{m}$ the imaging gradients become large enough that this decay is also affected by the dispersive motion of the fluid molecules.⁸⁷ In principle, such a multiecho PFG-NMR imaging experiment can relate an initial signal amplitude and a characteristic decay time to any pixel and value of \mathbf{R} . We used an additional multiecho imaging experiment (i.e., $\mathbf{q} = 0$) with increased signal-to-noise ratio (40 averages and 20 echoes) to examine the characteristic decay time for each pixel in the column. No systematic differences in decay times could be retrieved and we used the mean value (32 ms) to filter signals in the echo-train for each pixel in order to add filtered signals when needed and increase the signal-to-noise ratio of the final pixel propagators.

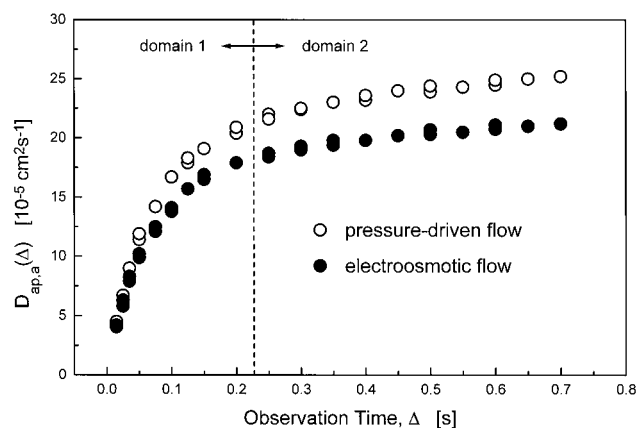


Figure 4. Observation time-dependence of the apparent axial dispersion coefficient $D_{ap,a}$ for electrokinetically and pressure-driven flows through the packed capillary at $Pe = Vd_p/D_m = 15$. $D_m = 2.25 \times 10^{-5} \text{ cm}^2 \text{ s}^{-1}$ (molecular diffusivity of pure water) and V is the mean velocity in the bed referring to its total porosity because the particles are porous.

Results and Discussion

The inherent length scales of axial and transverse fluid transport heterogeneities in fixed beds not only influence the asymptotic value of the axial dispersion coefficient (D_a) but also affect the time scale on which this value is approached at a given Peclet number (Pe). The ultimate goal in terms of dispersion is a rapid exchange ("equilibrium") of molecules moving in velocity extremes of the fluid flow field. It may be achieved by reducing associated correlation lengths in the bed and/or by fast lateral dispersion. In this respect, $Pe = Vd_p/D_m$ indicates the relative importance of convective and purely diffusive contributions.

Beginning with the temporal domain characterizing the transient dispersion, Figure 4 displays $D_{ap,a}$ as a function of time for electroosmotic and pressure-driven flows at $Pe = 15$, which is in a range typical for liquid chromatography ($5 < Pe < 20$). After a first, relatively steep increase up to ca. 250 ms (first domain), the curves level off and $D_{ap,a}$ seems to reach a plateau region. However, a closer look reveals that within this second domain the dispersion still increases in both types of liquid flow, i.e., $D_{ap,a}$ has not reached an asymptotic value yet and, in fact, it is not observed on the experimental time scale. In addition to this long-time tail ("disequilibrium") in the dispersion characteristics (it should be recalled that $D_{ap,a}$ itself is calculated from the NMR signal amplitude in the low- q limit by eq 11), Figure 5 shows corresponding, complete axial displacement probability distributions for EOF through the packed capillary. Propagator shapes for pressure-driven flow are qualitatively similar. They reveal features that have been reported earlier for nonporous particles.⁸⁸ Differences in the present work are due to the fact that the particles are totally porous, with an intraparticle porosity of about 0.65,⁸⁹ and that the aspect ratio is very low ($\psi = 5$). Thus, a contribution of wall effects (cf. Figures 1 and 2) to the studied macroscopic flow heterogeneity is aggravated.

At short times, the radially averaged axial displacement probability distribution mostly reflects the distribution of average velocity components in single pores of the porous medium (Figure 5a). It is caused by microscopic factors such as the random orientation of pores and differences in local morphology (permeability) or the electrokinetics (zeta-potential), depending on which type of flow we consider. While the diffusion length $L_D = (2D_m\Delta)^{1/2}$ in this flow regime may be sufficient to allow an exchange of velocities within the single pore, both L_D and the convective length $L_C = \bar{v}\Delta$ are typically smaller than the

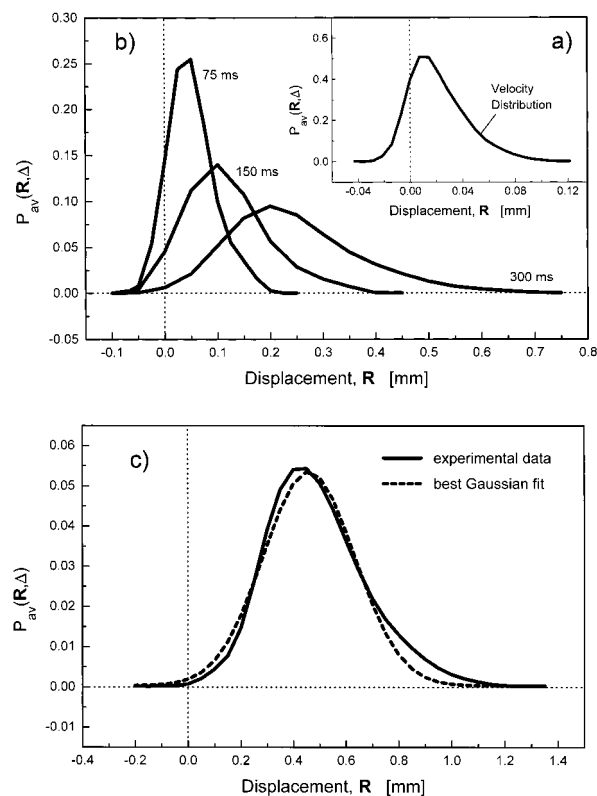


Figure 5. Radially averaged axial displacement probability distributions for EOF through the fixed bed in dependence of the observation time, $Pe = 15$. (a) $\Delta = 35$ ms, (b) Δ from 75 to 300 ms, and (c) $\Delta = 600$ ms. Electrical currents remained constant over the measurement periods within 3%.

longitudinal pore dimension, i.e., fluid molecules do not exchange between different pores (\bar{v} is the average pore velocity). Concluding from this microscopic viewpoint, $P_{av}(\mathbf{R}, \Delta) = P(\bar{v})$ also contains the complete velocity heterogeneity underlying the macroscopic flow profile. The highest average pore velocity that we calculate with Figure 5a (neglecting the fact that lateral diffusion over an L_D of 12 μm at $\Delta = 35$ ms has already achieved some exchange between flow velocities and thus blurs the clean velocity spectrum) is about 2.95 mm/s. This is quite a high (local) value, assuming that it originates in a straight pore between charged particles. Even when we take into account that the column cross-sectional averaged EOF (as compared to the straight single-pore geometry) is reduced by the tortuosity factor of the bed (approximately 0.6), this value remains much too high for typical cation exchange resins that have been used in CEC.^{90–92} It rather suggests that the high-velocity components observed in Figure 5a are associated with the fused-silica wall of the capillary. The values are, in fact, closer to those EOF velocities that have been obtained for open (fused-silica) capillaries using the same NMR approach and buffer; stronger thermal effects in the open tubular case caused by a Joule heating can explain most differences that may still exist.⁵¹ Thus, by knowing the typical EOF velocities in open and packed capillaries at sufficiently high ψ , already the one-dimensional propagator information allows to recognize larger displacements of fluid molecules close to the column wall moving in an annular region with a lateral dimension of the order of L_D , i.e., the distance that a molecule with \bar{v}_{max} at r_{eff} (eq 2) can diffuse along the radial velocity gradient.

Electrokinetic potentials at the inner wall of quartz capillaries up to -100 mV and even above are not unusual, although with the buffers and concentrations typically used in CEC the value

presents an upper limit and ζ_w usually ranges between -50 and -100 mV.^{93–96} By contrast, ζ_p of many commercial strong cation exchange particles such as those used in the present work can be significantly smaller than ζ_w of the bare fused-silica capillary,⁹¹ depending on the exact surface chemistry of the particle and associated electrokinetics. Thus, although these surfaces with sulfonic acid (cation exchange particle) and silanol groups (fused-silica capillary) both carry a negative charge density, the ratio ζ_w/ζ_p can be still substantial in current CEC practice (cf. Figure 2).^{90–92} In the extreme case that the particle surface does not generate an EOF, only the capillary inner surface may contribute to a volume flow,⁵⁴ if the resistance provided by the fixed obstacles does not prevent it completely. This also depends on the ratio of involved surface areas and consequently on ψ .

Yet another remark concerning the EOF behavior in porous media should be made at this point. It has been demonstrated that the equivalent radius of interstitial channels in packed beds (r_{inter}) is 25 to 40% of the particle radius,⁹⁷ i.e., $r_{\text{inter}} \approx 8 \mu\text{m}$ in the present work for $r_p = 25 \mu\text{m}$. Together with the buffer concentration (10^{-3} M), which gives κ^{-1} of the order of only 10 nm,³⁴ we are actually measuring in the limit of thin electrical double layers ($\kappa r_{\text{inter}} \gg 1$). In this regime, double-layer overlap in individual channels of the packed beds interstitial pore space is completely prevented (except at the contact points of particles) and the EOF should show a significantly superior performance compared to pressure-driven flows, including a relatively flat pore-level flow profile and average pore velocity that is rather independent of the pore radius (thus, also of the local packing homogeneity).^{46,93} As we have already seen in Figure 4, however, the axial dispersion characteristics of the EOF at long times are only moderately better than for pressure-driven flow (about 15%) when compared to the striking difference in a straight open capillary,^{50,51,98} and we demonstrate the main reason for it in due course.

By proceeding from Figure 5a, which indicates the distribution of average pore velocities via the exponential front of $P_{\text{av}}(\mathbf{R}, \Delta)$,⁸⁸ to Figure 5c, the observation time Δ is increased to 600 ms. The most striking result is that (in agreement with the data shown in Figure 4) a perfect Gaussian shape has not been reached after this long time, which, on a purely diffusive basis, translates to an L_D of ca. $50 \mu\text{m}$. It is evident that a disequilibrium in the fluid molecule axial displacement probability distribution must remain, $P_{\text{av}}(\mathbf{R}, \Delta)$ shows still substantial fronting. In the literature dealing with non-Gaussian dispersion in porous media, usually two mechanisms are discussed in that context: trapping of fluid molecules in stagnant zones and macroscopic flow heterogeneity.^{58,99} However, in contrast to some consolidated porous media such as rocks or sintered glass beads, the packed beds typically used in modern liquid chromatography have a relatively discrete time scale and length scale characterizing transport in stagnant zones and flow heterogeneity. The particles are spherical, with narrow size distribution.⁸⁵ Thus, the interstitial pores for flow are well connected, without particle cracks and fines, while stagnant zones are limited to the intraparticle pore space and hydrodynamic boundary layer that exists on the particle's external surface.

To specifically focus on macroscopic flow heterogeneity as a cause for the observed non-Gaussian behavior, we first study the characteristic time of stagnant mobile phase mass transfer for pressure-driven flow through the packed bed. It is achieved by selecting Pe high enough that moving and stagnant fluid can be quantitatively discriminated by eq 10, i.e., that the interstitial dispersion far exceeds intraparticle diffusion (cf. Figure 6a).

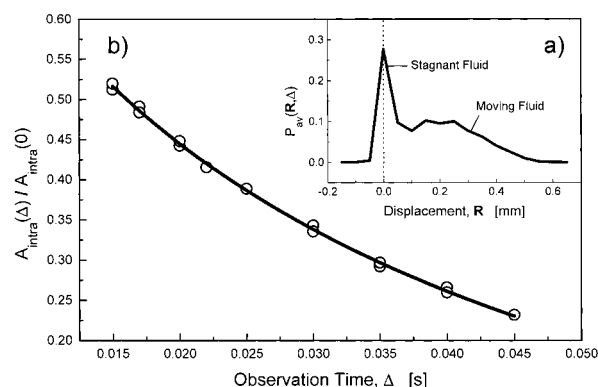


Figure 6. Stagnant mobile phase mass transfer for the 10^{-3} M sodium tetraborate buffer solution entrained in the deep pools of the cation exchange particles ($d_p = 50 \mu\text{m}$). (a) Averaged propagator distribution demonstrating stagnant and moving fluid fractions in the bed, $\Delta = 22$ ms. (b) Actual mass transfer kinetics and best fit of the data to eq 13 (solid line, $r^2 = 0.998$).

Then, with a series of measurements at increasing Δ , we determine $A_{\text{intra}}(\Delta)$, the amount of those fluid molecules that have remained purely diffusive inside the particles (in general, in any stagnant region of the medium as long as the characteristic dimension of that stagnant zone is much larger than L_D). By recording this fictitious emptying of the particles, we use that approach to calculate an intraparticle diffusion coefficient (D_{intra}) from the classical mass transfer rate constant^{74,100}

$$\frac{A_{\text{intra}}(\Delta)}{A_{\text{intra}}(0)} = \frac{6}{\pi^2} \sum_{n=1}^{\infty} \frac{1}{n^2} \exp\left(-n^2 \pi^2 \frac{D_{\text{intra}} \Delta}{r_p^2}\right) \quad (13)$$

The results of the analysis are shown in Figure 6b, and we see that the diffusion equation fits well the experimental data. Based on the intraparticle tortuosity factor (τ_{intra}), the average size and spherical shape of the particle diffusion-limited mass transfer should be finished after a characteristic exchange time (Δ_e), assuming that the molecules have to travel a net distance of $d_p/2$ to leave the porous particles completely

$$\Delta_e = \frac{\tau_{\text{intra}}}{2D_m} \left(\frac{d_p}{2}\right)^2 \text{ with } (\sqrt{\langle \mathbf{R}_{\text{intra}}^2 \rangle})_{\Delta=\Delta_e} = \frac{d_p}{2} \quad (14)$$

With eq 13 we find $D_{\text{intra}} = 1.34 \times 10^{-5} \text{ cm}^2 \text{ s}^{-1}$ ($\tau_{\text{intra}} = D_m/D_{\text{intra}} = 1.68$) and $\Delta_e = 233$ ms. Thus, the well-characterized stagnant mobile phase mass transfer in the packing (Figure 6) can be excluded as a cause for the transient dispersion behavior observed in domain 2 of Figure 4 and a corresponding non-Gaussian propagation of fluid molecules in Figure 5c. On the other hand, the temporal domain of this kinetics matches the time scale of domain 1 and, thus, may be responsible for most of the steep increase in $D_{\text{ap,a}}(\Delta)$. Actually, the dotted line in Figure 4 indicates the time when stagnant mobile phase mass transfer is complete for pressure-driven flow. This behavior is in contrast to nonporous particles for which an asymptotic dispersion, i.e., a transition from stationary random flow to pseudo-diffusion, is reached much faster than with porous ones,⁶⁴ because the holdup contribution is simply not present.⁷¹ In this respect it has been indicated that correlation times for nonmechanical dispersion mechanisms (holdup and boundary-layer dispersion) are long diffusive times and that transient effects associated with nonmechanical dispersion are more persistent than those associated with mechanical dispersion, i.e.,

with the dispersion due to velocity fluctuations in the bulk fluid induced by the randomly distributed particles.⁶²

In the present case, however, we also expect substantial macroscopic flow heterogeneity for EOF and pressure-driven flows through the bed (Figures 1 and 2). The length scales coupled to this nonuniformity of the flow pattern may spread over the whole capillary radius and by far exceed those associated with the stagnant mobile phase mass transfer (in which case it is just the particle radius). Then, the time needed to achieve an exchange of fluid molecules moving in the center of the bed and at the wall by lateral diffusion (or, more correctly, lateral dispersion at the actual Pe , because $D_t > D_m/\tau_{bed}$) can be a few seconds for $r_c = 125\ \mu\text{m}$. The situation becomes more severe for slowly diffusing biomolecules ($D_m < 10^{-7}\ \text{cm}^2\ \text{s}^{-1}$). It implies that through the involved transcolumn correlation length a macroscopic flow heterogeneity is responsible for the most persistent transient dispersion component (Figures 4 and 5), similar to the preasymptotic regime of Taylor–Aris dispersion in an open tube (although it shall by no means imply that the actual flow profiles are similar).^{51,101} For the latter case of a transcolumn equilibration, a perfect Gaussian displacement distribution is observed only when $L_D \geq r_c$.¹⁰² In the case of fixed beds, on the other hand, this length scale (r_c) may be covered faster due to lateral dispersion and the “diffusion” length becomes $L_D = (2D_t\Delta)^{1/2}$. By applying the magnetic field gradients perpendicular to the flow direction we can measure transverse dispersion and find $D_{ap,t} = 2.64 \times 10^{-5}\ \text{cm}^2\ \text{s}^{-1}$ at $\Delta = 600\ \text{ms}$ and $Pe = 15$ (cf. domain 2, Figure 4). Concerning its flow rate dependence, $D_{ap,t}(\Delta)$ has just left the so-called tortuosity-limited dispersion regime characterized by $D_m/\tau_{bed} < D_t < D_m$.

The value of $D_{ap,t}(\Delta)$ is almost an order of magnitude smaller than $D_{ap,a}(\Delta)$ and translates to an L_D of only $56\ \mu\text{m}$. Although it slightly exceeds purely diffusive mass transfer, this distance is by far not enough to allow the lateral dispersion of fluid molecules over the whole column radius. Consequently, features of a macroscopic flow heterogeneity such as transient dispersion and an associated non-Gaussian distribution of the fluid-element displacements will persist at corresponding observation times (as evident in Figures 4 and 5).

Still another detail (Figure 5c) suggests that some macroscopic flow heterogeneity of a type indicated by Figures 1 and 2 is responsible for the non-Gaussian distribution of fluid-element displacements (when $L_D < r_c$). We generally observed no tailing but fronting in $P_{av}(\mathbf{R},\Delta)$, which implies the existence of a substantial region in both electroosmotic and pressure-driven flows with higher-than-average velocity (the “true” average refers to a packed segment without wall effect, i.e., to an infinite-diameter bed). By contrast, the large heterogeneities caused by low-permeability zones in which the velocity is not necessarily zero and by purely diffusive zones (especially important for porous media near the percolation threshold or very slowly diffusing solutes which strongly adsorb on the surface) usually give rise to tailing.^{57,58} We now tried to spatially resolve these wall effects by dynamic NMR microimaging with in-plane resolution of $40\ \mu\text{m}$. The slice thickness was set to $6\ \text{mm}$ because we expect the effects to be systematic along the column axis and consequently do not require a high spatial resolution in this third dimension. Thus, a reasonable signal-to-noise ratio and a sufficiently high resolution over the column cross-section (compared to the particle diameter, $d_p = 50\ \mu\text{m}$) could be achieved.

The results of this microscopic investigation are summarized in Figures 7 and 8. The single-pixel propagator distributions in

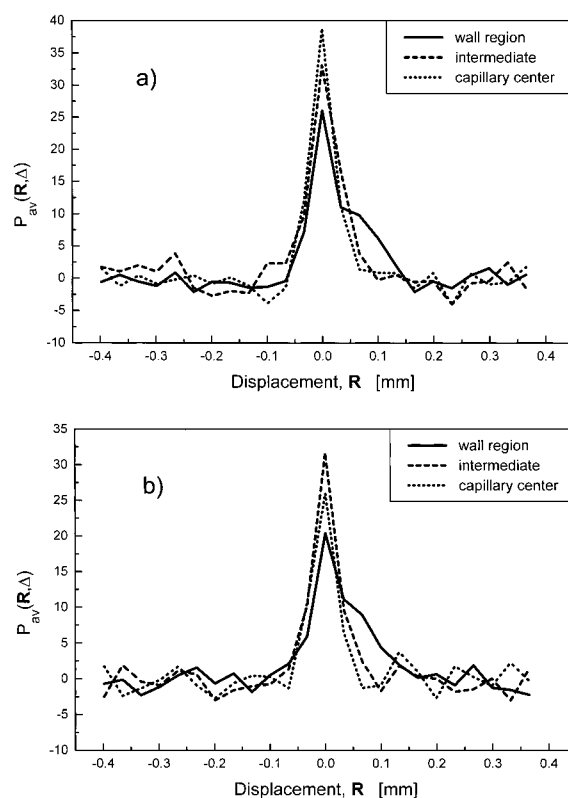


Figure 7. Axial displacement probability distribution for fluid molecules in single pixels of the image. (a) EOF and (b) pressure-driven flow through the packed capillary ($\Delta = 17.5\ \text{ms}$). Pixels are taken along a straight line through the center, wall, and intermediate region of the column cross-section. For experimental parameters refer to Figure 3.

Figure 7 clearly reveal a substantial increase of fluid velocity close to the column wall as compared to the center of the bed. It seems that the macroscopic flow heterogeneities in electroosmotic and pressure-driven flows extend even further inward from the wall to pixels at intermediate positions and thus may cover length scales of the order of the column radius in the present case with $\psi = 5$. The propagators from four added pixels representative of wall and center positions are shown in Figure 8. Data were collected from opposite edges of the capillary cross-section (wall region 1 and 2), and, in contrast to $P_{av}(\mathbf{R},\Delta)$ in Figure 7, they are zero-filled and normalized. The distributions show pronounced shoulders or even separate local maxima for fluid molecules in pixels closer to the column wall and the effects scale with observation time (Figures 8a and 8b), but a lateral exchange of molecules between velocity extremes is also promoted. Thus, pore-level velocities become increasingly blurred as we approach equilibrium in the mobile phase.

In both types of flow, we observe higher velocities as we move toward the wall, although at this stage it is difficult to say whether the effects are more severe in EOF than for pressure-driven flow because the difference in $D_{ap,a}(\Delta)$ remains small at the observation times used to acquire the data shown in Figures 7 and 8 (domain 1, Figure 4). Yet, they have a completely different origin, but in both cases contribute substantially to the interstitial dispersion. At this stage, however, it is more important that the high-velocity components seen in these imaging studies close to the capillary wall compare well with top velocities in the exponential front of the 1-D propagators (Figure 5a), which a priori have been blamed on the fused-silica wall (via ζ_w). The results confirm that a first insight into the magnitude of EOF velocities in the critical wall region can

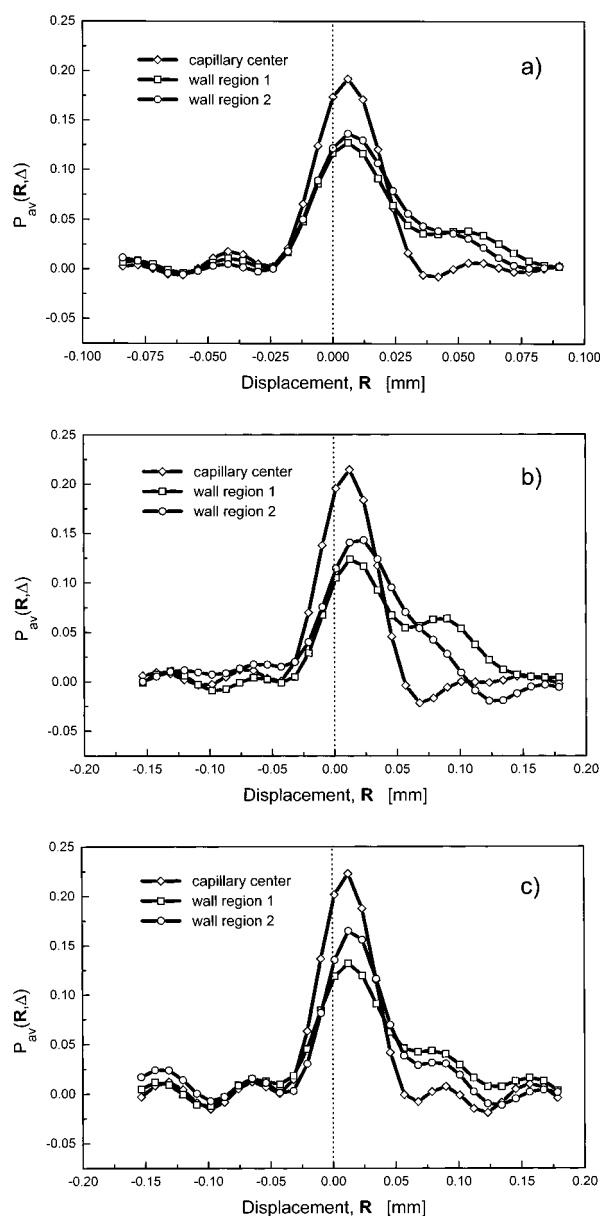


Figure 8. Added propagators comparing the fluid dynamics in wall and center positions of the capillary for EOF: (a) $\Delta = 17.5$ ms and (b) $\Delta = 35$ ms, and pressure-driven flow (c) $\Delta = 35$ ms. Displacement distributions have been normalized by their surface area. Mobile phase: 10^{-3} M sodium tetraborate buffer (pH 9.13).

already be gained from the 1-D data, with measurement times of 10 min only. Ongoing studies that could help to distinguish further between these macroscopic flow heterogeneities could employ matched surface potentials ($\zeta_w \approx \zeta_p$) while keeping ψ constant and, thus, leaving the wall effect critical for pressure-driven flow, but minimizing it with EOF.

Conclusions

Our results demonstrate that a significantly superior performance, which has been shown for EOF through packed capillaries^{35–39} compared to pressure-driven flows, can be obstructed by wall effects, and it is difficult to trace back remaining differences in the asymptotic dispersion observed for these types of fluid flow to an inherent performance concerning intraparticle and film mass transfer or a macroscopic flow heterogeneity. NMR microscopy and PFG-NMR are techniques

by which the physical mechanisms that contribute to dispersion in the flowing and stagnant zones of the bed may be addressed separately.

The influence of the documented electrokinetic wall effect in current CEC practice ($\psi < 50$) is two-fold. First, depending on the ratios d_c/d_p and ζ_w/ζ_p , it contributes to the long-time averaged velocity through the packed capillary. Second, it engenders additional band spreading. Even if the aspect ratio can be increased and the first consequence be neglected, systematic offsets in zeta-potential remain and sensitively influence eddy-dispersion. This particular contribution can be eliminated only when $\zeta_w \approx \zeta_p$ and is rather important to consider in CEC where particle technology has begun to focus on electrokinetics in more detail.³⁹

The operation with pressure-driven flows in packed capillaries is limited by the back pressure of the beds. For this reason, aspect ratios typically used in CHPLC are below 50. Wall effects are caused by the radial distribution of porosity, which has been extensively studied for larger columns.^{1–16} The problems encountered with particulate packings in CHPLC and CEC can be overcome by the use of monoliths.^{103–105} They are fabricated as a continuous porous medium with small domain size of the solid or porous fractal skeleton, but relatively large flow-through pores, providing low pressure-drops and high column efficiency. In view of the zeta-potential and CEC applications, the capillary inner wall may be coated by a fluid-impervious annulus of the same material, thus reducing the excess zeta-potential between wall (usually fused-silica) and monolithic material.

Acknowledgment. We gratefully acknowledge the award of a Marie Curie Fellowship (U.T.) under the Training and Mobility of Researchers Program from the European Union (Contract ERBFMBI-CT98-3437). This research was further supported by the European Community activity Large-Scale Facility Wageningen NMR Centre (Contract ERBCHGE-CT95-0066), by the Technology Foundation STW (Project WBI.3493), Applied Science Division of the Dutch Science Foundation NWO, and the Deutsche Forschungsgemeinschaft DFG (Grant SE 586/7-1). We thank Erdmann Rapp (Otto-von-Guericke Universität Magdeburg, Germany) for preparing the packed capillary.

References and Notes

- Schertz, W. W.; Bischoff, K. B. *AIChE J.* **1969**, *15*, 597.
- Lerou, J. J.; Froment, G. F. *Chem. Eng. Sci.* **1977**, *32*, 853.
- Pillai, K. K. *Chem. Eng. Sci.* **1977**, *32*, 59.
- Schuster, J.; Vortmeyer, D. *Chem. Eng. Technol.* **1981**, *53*, 806.
- Vortmeyer, D.; Schuster, J. *Chem. Eng. Sci.* **1983**, *38*, 1691.
- Vortmeyer, D.; Michael, K. *Chem. Eng. Sci.* **1985**, *40*, 2135.
- Govindarao, V. M. H.; Froment, G. F. *Chem. Eng. Sci.* **1986**, *41*, 533.
- Ziolkowska, I.; Ziolkowski, D. *Chem. Eng. Process.* **1988**, *23*, 137.
- Daszkowski, T.; Eigenberger, G. *Chem. Eng. Sci.* **1992**, *47*, 2245.
- Legawiec, B.; Ziolkowski, D. *Chem. Eng. Sci.* **1994**, *49*, 2513.
- Papageorgiou, J. N.; Froment, G. F. *Chem. Eng. Sci.* **1995**, *50*, 3043.
- Bey, O.; Eigenberger, G. *Chem. Eng. Sci.* **1997**, *52*, 1365.
- Giese, M.; Rottschäfer, K.; Vortmeyer, D. *AIChE J.* **1998**, *44*, 484.
- Roblee, L. H. S.; Baird, R. M.; Tierney, J. W. *AIChE J.* **1958**, *4*, 460.
- Benenati, R. F.; Brosilow, C. B. *AIChE J.* **1962**, *8*, 359.
- Ridgway, K.; Tarbuck, K. J. *Chem. Eng. Sci.* **1968**, *23*, 1147.
- Brinkman, H. C. *Appl. Sci. Res.* **1947**, *A1*, 27.
- Ergun, S. *Chem. Eng. Prog.* **1952**, *48*, 89.
- Hsiang, T. C.; Haynes, H. W., Jr. *Chem. Eng. Sci.* **1977**, *32*, 678.
- Martin, H. *Chem. Eng. Sci.* **1978**, *33*, 913.
- Carbonell, R. G. *Chem. Eng. Sci.* **1980**, *35*, 1347.
- Ahn, B.-J.; Zoulalian, A.; Smith, J. M. *AIChE J.* **1986**, *32*, 170.
- Gunn, D. J.; Price, C. *Trans. Inst. Chem. Eng.* **1969**, *47*, 341.
- Guiochon, G.; Farkas, T.; Guan-Sajonz, H.; Koh, J.-H.; Sarker, M.; Stanley, B. J.; Yun, T. J. *Chromatogr. A* **1997**, *762*, 83.

- (25) Guiochon, G.; Drumm, E.; Cherrak, D. *J. Chromatogr. A* **1999**, 835, 41.
- (26) Shalliker, R. A.; Broyles, B. S.; Guiochon, G. *J. Chromatogr. A* **2000**, 888, 1.
- (27) Sarker, M.; Katti, A. M.; Guiochon, G. *J. Chromatogr. A* **1996**, 719, 275.
- (28) Train, D. *Trans. Inst. Chem. Eng.* **1957**, 35, 258.
- (29) Yuan, Q. S.; Rosenfeld, A.; Root, T. W.; Klingenberg, D. J.; Lightfoot, E. N. *J. Chromatogr. A* **1999**, 831, 149.
- (30) Knox, J. H.; Laird, G. R.; Raven, P. A. *J. Chromatogr.* **1976**, 122, 129.
- (31) Eon, C. H. *J. Chromatogr.* **1978**, 149, 29.
- (32) Farkas, T.; Sepaniak, M. J.; Guiochon, G. *AIChE J.* **1997**, 43, 1964.
- (33) Probstein, R. F. *Physicochemical Hydrodynamics: An Introduction*; John Wiley & Sons: New York, 1994.
- (34) Lyklema, J. *Fundamentals of Interface and Colloid Science, Vol. II: Solid-Liquid Interfaces*; Academic Press: London, 1995.
- (35) Dittmann, M. M.; Wienand, K.; Bek, F.; Rozing, G. P. *LC-GC* **1995**, 13, 800.
- (36) Crego, A. L.; González, A.; Marina, M. L. *Crit. Rev. Anal. Chem.* **1996**, 26, 261.
- (37) Colón, L. A.; Reynolds, K. J.; Alicea-Maldonado, R.; Fermier, A. M. *Electrophoresis* **1997**, 18, 2162.
- (38) Fujimoto, C. *TrAC - Trends Anal. Chem.* **1999**, 18, 291.
- (39) Colón, L. A.; Burgos, G.; Maloney, T. D.; Citrón, J. M.; Rodríguez, R. L. *Electrophoresis* **2000**, 21, 3965.
- (40) Tsuda, T. *Anal. Chem.* **1987**, 59, 521.
- (41) Knox, J. H. *J. Chromatogr. A* **1994**, 680, 3.
- (42) Knox, J. H. *Chromatographia* **1988**, 26, 329.
- (43) Patankar, N. A.; Hu, H. H. *Anal. Chem.* **1998**, 70, 1870.
- (44) Rathore, R. S.; Horváth, Cs. *Anal. Chem.* **1998**, 70, 3069.
- (45) Dresner, L. *J. Phys. Chem.* **1963**, 67, 1635.
- (46) Rice, C. L.; Whitehead, R. *J. Phys. Chem.* **1965**, 69, 4017.
- (47) Gross, R. J.; Osterle, J. F. *J. Chem. Phys.* **1968**, 49, 228.
- (48) Sims, S. M.; Higuchi, W. I.; Srinivasan, V.; Peck, K. J. *Colloid Interface Sci.* **1993**, 155, 210.
- (49) Arulanandam, S.; Li, D. *Colloids Surf. A* **2000**, 161, 89.
- (50) Paul, P. H.; Garguilo, M. G.; Rakestraw, D. J. *Anal. Chem.* **1998**, 70, 2459.
- (51) Tallarek, U.; Rapp, E.; Scheenen, T.; Bayer, E.; Van As, H. *Anal. Chem.* **2000**, 72, 2292.
- (52) Knox, J. H.; Grant, I. H. *Chromatographia* **1991**, 32, 317.
- (53) Rathore, R. S.; Horváth, Cs. *J. Chromatogr. A* **1997**, 781, 185.
- (54) Liapis, A. I.; Grimes, B. A. *J. Chromatogr. A* **2000**, 877, 181.
- (55) Neale, G.; Epstein, N.; Nader, W. *Chem. Eng. Sci.* **1973**, 28, 1865.
- (56) Unger, K. K.; Lüdtkke, S.; Grün, M. *LC-GC Int.* **1999**, 12, 870.
- (57) Sahimi, M. *Flow and Transport in Porous Media and Fractured Rock: From Classical Methods to Modern Approaches*; VCH: Weinheim, 1995.
- (58) Salles, J.; Thovert, J.-F.; Delannay, R.; Prevors, L.; Auriault, J.-L.; Adler, P. M. *Phys. Fluids A* **1993**, 5, 2348.
- (59) Bear, J. *Dynamics of Fluids in Porous Media*; Dover Publications: New York, 1988.
- (60) Koch, D. L.; Cox, R. G.; Brenner, H.; Brady, J. F. *J. Fluid Mech.* **1989**, 200, 173.
- (61) Koch, D. L.; Brady, J. F. *J. Fluid Mech.* **1987**, 180, 387.
- (62) Koch, D. L.; Brady, J. F. *Chem. Eng. Sci.* **1987**, 42, 1377.
- (63) Ding, A.; Candela, D. *Phys. Rev. E* **1996**, 54, 656.
- (64) Seymour, J. D.; Callaghan, P. T. *AIChE J.* **1997**, 43, 2096.
- (65) Amin, M. H. G.; Gibbs, S. J.; Chorley, R. J.; Richards, K. S.; Carpenter, T. A.; Hall, L. D. *Proc. R. Soc. London A* **1997**, 453, 489.
- (66) Tallarek, U.; Bayer, E.; Guiochon, G. *J. Am. Chem. Soc.* **1998**, 120, 1494.
- (67) Stapf, S.; Packer, K. J.; Graham, R. G.; Thovert, J.-F.; Adler, P. M. *Phys. Rev. E* **1998**, 58, 6206.
- (68) Stapf, S.; Packer, K. J.; Békri, S.; Adler, P. M. *Phys. Fluids* **2000**, 12, 566.
- (69) Sederman, A. J.; Johns, M. L.; Alexander, P.; Gladden, L. F. *Chem. Eng. Sci.* **1998**, 53, 2117.
- (70) Manz, B.; Alexander, P.; Gladden, L. F. *Phys. Fluids* **1999**, 11, 259.
- (71) Van As, H.; Palstra, W.; Tallarek, U.; van Dusschoten, D. *Magn. Reson. Imaging* **1998**, 16, 569.
- (72) Manz, B.; Gladden, L. F.; Warren, P. B. *AIChE J.* **1999**, 45, 1845.
- (73) Tallarek, U.; van Dusschoten, D.; Van As, H.; Guiochon, G.; Bayer, E. *Angew. Chem., Int. Ed. Engl.* **1998**, 37, 1882; *Angew. Chem.* **1998**, 110, 1983.
- (74) Tallarek, U.; Vergeldt, F. J.; Van As, H. *J. Phys. Chem. B* **1999**, 103, 7654.
- (75) Callaghan, P. T.; MacGowan, D.; Packer, K. J.; Zelaya, F. O. *J. Magn. Reson.* **1990**, 90, 177.
- (76) Callaghan, P. T.; Coy, A.; MacGowan, D.; Packer, K. J.; Zelaya, F. O. *Nature* **1991**, 351, 467.
- (77) Cotts, R. M. *Nature* **1991**, 351, 443.
- (78) Kärgner, J.; Heink, W. *J. Magn. Reson.* **1983**, 51, 1.
- (79) Kärgner, J.; Pfeiffer, H.; Heink, W. *Adv. Magn. Reson.* **1988**, 12, 1.
- (80) Stejskal, E. O.; Tanner, J. E. *J. Chem. Phys.* **1965**, 42, 288.
- (81) Stejskal, E. O. *J. Chem. Phys.* **1965**, 43, 3597.
- (82) Callaghan, P. T.; Stepišnik, J. *Adv. Opt. Magn. Reson.* **1996**, 19, 325.
- (83) Callaghan, P. T.; Xia, Y. *J. Magn. Reson.* **1991**, 91, 326.
- (84) Callaghan, P. T. *Principles of Nuclear Magnetic Resonance Microscopy*; Clarendon Press: Oxford, 1993.
- (85) Neue, U. D. *HPLC Columns: Theory, Technology, and Practice*; Wiley-VCH: New York, 1997.
- (86) van Dusschoten, D.; Moonen, C. T. W.; de Jager, P. A.; Van As, H. *Magn. Reson. Med.* **1996**, 36, 907.
- (87) Edzes, H. T.; van Dusschoten, D.; Van As, H. *Magn. Reson. Imaging* **1998**, 16, 185.
- (88) Lebon, L.; Leblond, J.; Hulin, J. P. *Phys. Fluids* **1997**, 9, 481.
- (89) Whitney, D.; McCoy, M.; Gordon, N.; Afeyan, N. *J. Chromatogr. A* **1998**, 807, 165.
- (90) Choudhary, G.; Horváth, Cs. *J. Chromatogr. A* **1997**, 781, 161.
- (91) Rathore, A. S.; Wen, E.; Horváth, Cs. *Anal. Chem.* **1999**, 71, 2633.
- (92) Liu, Y.; Pietrzyk, D. J. *Anal. Chem.* **2000**, 72, 5930.
- (93) Overbeek, J. Th. G. *Electrokinetic Phenomena*. In *Colloid Science*; Kruyt, H. R., Ed.; Elsevier: Amsterdam, 1952, Chapter 5.
- (94) Hunter, R. J.; Wright, H. J. L. *J. Colloid Interface Sci.* **1971**, 37, 564.
- (95) Vindevogel, J.; Sandra, P. *J. Chromatogr.* **1991**, 541, 483.
- (96) Tsuda, T. *Electroosmosis and Electrochromatography*. In *Electric Field Applications in Chromatography, Industrial and Chemical Processes*; Tsuda, T., Ed.; VCH: Weinheim, 1995; Chapter 3.
- (97) Dullien, F. A. L. *Porous Media: Fluid Transport and Pore Structure*; Academic Press: New York, 1992.
- (98) Griffiths, S. K.; Nilson, R. H. *Anal. Chem.* **1999**, 71, 5522.
- (99) Gist, G. A.; Thompson, A. H.; Katz, A. J.; Higgins, R. L. *Phys. Fluids A* **1990**, 2, 1533.
- (100) Crank, J. *The Mathematics of Diffusion*; Clarendon Press: Oxford, 1956, Chapter 6.
- (101) Codd, S. L.; Manz, B.; Seymour, J. D.; Callaghan, P. T. *Phys. Rev. E* **1999**, 60, R3491.
- (102) Golay, M. J. E.; Atwood, J. G. *J. Chromatogr.* **1979**, 186, 353.
- (103) Gusev, I.; Huang, X.; Horváth, Cs. *J. Chromatogr. A* **1999**, 855, 273.
- (104) Svec, F.; Fréchet, J. M. J. *Ind. Eng. Chem. Res.* **1999**, 38, 34.
- (105) Ishizuka, N.; Minakuchi, H.; Nakanishi, K.; Soga, N.; Nagayama, H.; Hosoya, K.; Tanaka, N. *Anal. Chem.* **2000**, 72, 1275.